

Numerical reproduction of OH* radiation measurements of unsteady supercritical LOx/H₂ combustion

Federica Tonti¹, José Zapata Usandivaras¹, Jaka Perovšek¹, Sebastian Karl², Justin S.Hardi¹, Michael Oschwald^{1,3}

Abstract

Radiation emitted from hydroxyl radicals (OH*) in high pressure oxygen-hydrogen flames has often been used as a marker for the flame zone because it is a physical quantity which is relatively easy to capture experimentally with high-speed cameras or photomultipliers. However, quantitative comparison of CFD results with experimental data and its use as an indicator of heat release during the combustion process is still an open problem. In order to compare CFD simulation results with experimental data, a radiation modelling tool has been developed at the Institute of Space Propulsion at the German Aerospace Center (DLR). This tool takes as input the relevant field variables obtained by a CFD simulation and gives as an output the intensity of the radiation emitted by OH* molecules as a result of the thermal excitation of OH ground state molecules by applying a reverse ray-tracing algorithm. This work aims to investigate the flame response of a single injector element fed with LOx/H₂ subject to acoustic forcing and the fluctuations of the intensity of the OH* radiation emitted from the flame. The results are then compared with experimental data. The main steps are running a URANS simulation and investigate the flame response to acoustic excitation and apply the radiation modelling and ray-tracing tool to extract the OH* radiation intensity fluctuations recorded by an optical probe of the chamber. The results show a good qualitative agreement with the experimental data and give better understanding of the flame dynamics giving rise to inherently nonlinear radiation intensity dynamics.

Keywords

Radiation modelling, High pressure combustion, High frequency combustion instabilities, OH* radiation

Introduction

High frequency (HF) combustion instabilities are an ongoing challenge to the development of rocket combustion chambers. The occurring of the phenomenon is triggered by the coupling of pressure oscillations and unsteady energy release which derives from the combustion process. The coupling leads to an unsteady heat release rate and the phenomena close in a loop. Numerical simulations are a promising tool for the investigation of such phenomena as much as for design purposes. To validate such tools, a comparison between the results of simulations and experimental data is necessary. The experimental detection of the physical properties of the flames is a challenging task, especially for liquid propellant rocket engines (LPRE), because of the extreme conditions at which they operate. During the combustion process very high temperatures and pressures are reached, and the detection of important combustion parameters, for example mass fractions of the involved species or temperature is difficult due to this unfriendly environment. It is then necessary to focus on quantities which can be given as results of a numerical simulation and are easily comparable with experimental data. A suitable physical parameter for this comparison is the radiation emitted from the flame, which is often used as a marker of the flame zone. In particular, when dealing with LOx/H₂ flames, the radiation emitted by the excited hydroxyl radical (OH*) can be used for this purpose.

OH* radiation has been used often to identify flame emission zones in high temperature flames^{1,2} because it is clearly distinguishable in the UV spectrum range with respect to other radiating sources, being the central wavelength at 310 nm³. Chemiluminescence of excited radicals, which originates from the relaxation of electronically excited species produced by the combustion reaction in the flame, has been used to study light emission taking place in the reaction zone, providing information about the energy release in the flame radiation zone. However, the fundamental parameter to study combustion instabilities is the volumetric heat release rate \dot{q} , which cannot be measured experimentally. For this reason, many studies have been focusing on determining whether there can be a quantitative correlation between flame radiation and heat release rate to study combustion instabilities or not.

¹DLR-Institute of Space Propulsion, Im Langen Grund, 74239 Hardthausen am Kocher, Germany

²DLR-Institute of Aerodynamics and Flow Technology, Bunsenstrasse 10, 32073, Göttingen, Germany

³RWTH Aachen University, Institute of Jet Propulsion and Turbomachinery, Templergraben 55, 52062, Aachen, Germany

Corresponding author:

Federica Tonti, DLR-Institute of Space Propulsion, Im Langen Grund, 74239 Hardthausen am Kocher, Germany

Email: federica.tonti@dlr.de

Emission of radicals as an indicator of the heat release rate was first investigated in real and experimental combustion^{4,5}. In order to define whether OH* radiation (and also CH* in hydrocarbon flames) could be an indicator of heat release, many studies have been involved⁶⁻¹⁶ with the goal to state if a quantitative correlation between OH* radiation and heat release rate is possible. In all of these works, it is assumed chemiluminescence takes place where the heat release rate is defined from chemical reactions, and the use of chemiluminescence as a marker for the heat release is made on a case-by-case basis, with different results depending on strain rate of the flame, degree of turbulence, degree of premixing, pressure and equivalence ratio. Chemiluminescence of CH* and OH* in a methane flame was investigated both experimentally and numerically in a recent work of Bedard et al.¹ with a detailed chemical scheme for methane. It is shown that, although a detailed chemical reaction scheme was used for methane, the ratio of emission intensity between OH* and CH* is greater than the one observed in experiments. This is due to self-absorption which causes distortion in the line-of-sight measurements. A spatial correlation of heat release and radiation was observed by comparing experimental data and simulations, but both CH* and OH* radiation are not sufficient to resolve the spatial and temporal distribution of the heat release. In this work, thermal excitation was completely neglected.

Here, the focus is on thermal excitation of OH molecules produced during the combustion process of LOx and H₂. Very little literature is available regarding high pressure and temperature flames. Generally, for relatively cold flames with temperatures below 2700 K, it is reasonable to take into account only chemical excitation of the molecules, but above this threshold, thermal excitation becomes predominant as shown by Fiala¹⁷. Moreover, thermal equilibrium between OH and OH* is assumed. This is the main assumption of the Equilibrium Filtered Radiation Model (EFRM) of Fiala¹⁷. Experimentally, the relation between heat release and OH* radiation has not been discussed in detail for non-premixed O₂/H₂ flames. The only work is the one of Burrows¹⁸, which used OH* radiation to determine the reaction zone.

When studying flame radiation, taking into account self-absorption is crucial. Self-absorption is the phenomenon which takes place when the radiation emitted from the molecules is subject to the absorption by the same molecules which are present in the ground state. Neglecting self-absorption can lead to an important overestimation of the calculated radiance, as shown in Perovšek¹⁹. Another important phenomenon to consider in high pressure and temperature flames is refraction. Refraction is the bending of a ray of light when it passes from one medium to another. The bending is caused by the differences in density between the media where the rays pass through. This can be included using ray-tracing algorithms, where refraction is modeled.

The goal of this work is to show how a tool which models self-absorption and refraction can capture the fluctuations of the radiation emitted by OH* molecules in a flame when exposed to acoustic forcing, and further investigate the relation between heat release rate and radiation in the flame response. This is done in a post-processing step to avoid the computational cost of modeling the production of

OH* molecules at runtime. The tool is applied to the HF-9 REST test case. Here an optical probe has to be modelled to correctly capture the total radiance emitted from the flame. The view angle of the optical probe is different from zero and the rays cannot be approximated as parallel when reaching the detector surface.

The next section describes the tool in detail and the equations implemented. Then, the methodology and logic of the simulations will be presented, with a short description of the modelling of the optical probe. Finally, the section of results will show the main results of the simulation.

Radiation modelling and ray-tracing

The ray tracing routine approximates the behaviour of the light emitted by the excited OH* molecules by assuming the principles of geometrical optics with modelled refraction caused by density gradients. The calculations are spectrally resolved in a range of wavelengths from 305 nm to 320 nm, which accounts for self-absorption phenomena. This is crucial to model correctly the radiation of flames where OH is present as a combustion product in high concentrations. Previous studies underlined that self-absorption affects the flame radiation considerably with increasing pressures^{17,20,21}. Diffraction, refraction, scattering and blackbody radiation from walls and gases are neglected. The algorithm takes the data coming from a CFD solution as input. In this case the CFD solution was generated with the in-house DLR TAU code. The data are treated as a quasi-continuum with an inverse distance interpolation based on nearest neighbours. First, the calculation of the refractive index n for each vertex of the considered CFD solution domain is performed using the Gladstone-Dale relation²²:

$$n(T, p) = 1 + \rho(T, p) \cdot k \quad (1)$$

Here, T denotes the temperature, p the pressure, ρ the density and k the Gladstone-Dale coefficient. For mixtures of fluids with different atomic and molecular species the representative Gladstone-Dale coefficient $\bar{k} = \sum k_i \cdot x_i$ is used, where k_i is the Gladstone-Dale coefficient of the species i and x_i the molar fraction of the species at the evaluated point. In order to obtain the pseudo-OH* images, the definition of the points where the rays are expected to enter a detector by the position vector $\mathbf{r} = [r_x, r_y, r_z]^T$ and the unit vector $\mathbf{T} = [T_x, T_y, T_z]^T$ which correspond to the opposite direction of the light that would enter a detector is necessary. Integrating the eikonal equation, each ray is obtained. The eikonal equation describes the electromagnetic wave propagation on a path s under the assumption of geometrical optics in a scalar field $n(\mathbf{r})$ of continuously changing refractive index n ²³:

$$\frac{d}{ds} \left[n(\mathbf{r}) \frac{d\mathbf{r}}{ds} \right] = \nabla n(\mathbf{r}) \quad (2)$$

Then equation 2 is split into two differential equations of first order and solved using the Runge-Kutta method of order five:

$$\frac{d\mathbf{r}}{ds} = \frac{\mathbf{T}}{n(\mathbf{r})} \quad (3)$$

$$\frac{d\mathbf{T}}{ds} = \nabla n(\mathbf{r}) \quad (4)$$

Here, \mathbf{r} and \mathbf{T} are part of the vectors of initial conditions required by the solver. The solver stops as soon as the calculated position vector $\mathbf{r}(s)$ is outside of defined geometry boundaries and then outputs a solution set of vectors $[\mathbf{r}(s=0) \dots \mathbf{r}(s=s_{\text{end}})]^T$ that represent the points on the ray. The thermodynamic properties (temperature T , pressure p and a set of mass fractions $X = [w_{H_2}, w_{H_2O}, w_{O_2}, w_{OH}]$) at the vertices of the grid elements along the ray are obtained by interpolation once the solution of the ray is available. They serve as inputs for a routine that determines the emission spectrum e_λ and absorption spectrum κ_λ for their respective points. Subsequently, the radiative transfer equation is solved in the spectral range of interest (305-320 nm) for each wavelength starting from the physical origin of the ray towards the detector. The obtained spectral radiance is then multiplied with the transmittance of the OH* filter. The next step is integrate the spectral filtered radiance over the wavelength range 305-320 nm using Simpson's rule, and the spectral radiance is obtained for all the points of interest on a single ray. The tool developed following this procedure is named Spectral Modelling And Ray Tracing (SMART) tool.

HF-9 Test case description

The test case to which SMART is applied is the one presented in the frame of the 4th modelling workshop of the REST community. The focus of the modelling workshop was the combustion chamber D (BKD), operated at the test bench P8 at DLR Institute of Space Propulsion in Lampoldshausen. It is a cylindrical combustor which shows self-excited combustion instabilities at certain load points. The injector head has 42 shear coaxial injectors and combustion chamber pressure can reach up to 80 bar. The chamber has a diameter of 80 mm, the injectors have a recess of 2 mm and a taper angle of 5 degrees. The measurement ring is equipped with eight dynamic pressure sensors which are installed and flush mounted at equiangular positions along the circumference of the measurement ring. The measurement plane of the ring is 5.5 mm downstream the faceplate. Figure 1 shows the BKD geometry.

The measurement ring is equipped with three optical probes. Figure 2 shows the position of the probes together with the line of sight and collection angle.

The fields of view of the probes are aligned in different ways with respect to the outer row of injectors. One probe is aligned with the axis of an outer element, the other two are aimed along a tangent of the LOx post, with the line of sight passing through the shear layer between oxygen and hydrogen streams. Light from the combustion chamber enters the probes and passes into an optical fibre. Upon exiting the optical fibre the light passes through an interference filter with a pass band in the UV wavelength range of 305-315 nm. The filtered light is collected by a photomultiplier and the voltage output signal is recorded with a sampling rate of 100 kHz. The effective frequency

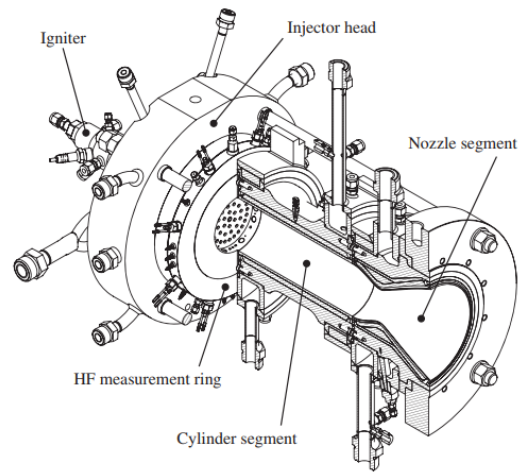


Figure 1. Combustion Chamber BKD

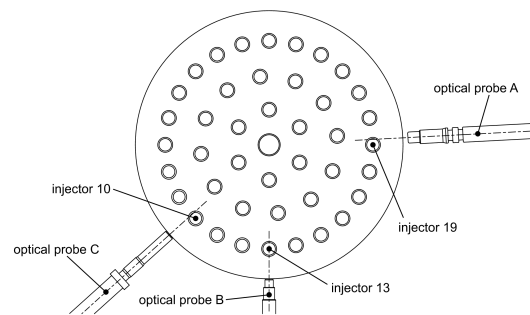


Figure 2. Alignment of optical probes

response range of the photomultipliers is up to approximately 30 kHz. For the chosen load point, the 1T mode shows self-excited combustion instability with an amplitude of 3.4 bar.

The data collected by the optical probes show that the combustion dynamics is dominated by the LOx post resonant frequencies²⁴, which are multiples of 5 kHz. However, from the experiment it was unclear how the flame was modulated by the dominant frequencies. This gives a motivation for the use of a URANS simulation, in order to investigate more in detail the flame dynamics. Another feature of the selected load point is the interaction of the 1T mode of the chamber and 2L mode of the LOx post, as they are very close in frequency, with a difference below 200 Hz. Moreover, in the experiment, OH* fluctuations and acoustic pressure fluctuations are mostly in phase for the described unstable conditions.

Numerical Modelling

First, a steady state simulation (RANS) under the prescribed operating conditions is run. Then, for the BKD case an unsteady simulation (URANS) is run in order to investigate the flame response under excitation in a representative sub-domain of the combustion chamber containing the flame from a single injector. The final step is the application of SMART with the production of pseudo-OH* images and the evaluation of the intensity at one of the probe locations in BKD. The images and signals obtained are then compared with the experimental data. The simulations are run with DLR in-house code TAU, a 2D axisymmetric single injector

subdomain was chosen. The radius of the representative chamber volume is 6.2 mm to make the area swept from the radius be 1/42 of the real chamber cross section, and the domain includes the oxygen dome and orifice. The choice of subdomain and axisymmetric model was made in order to reduce the computational time and costs of the simulation for the unsteady case and it is justified because the wavelength of the 1T mode is much greater than the dimensions of the single injector. Figure 3 shows the computational domain and boundary conditions adopted for the RANS simulation.

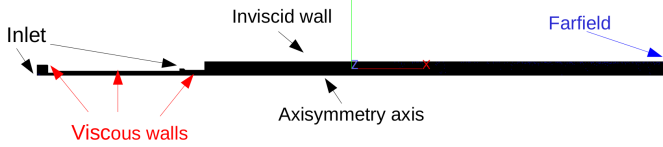


Figure 3. 2D computational domain and boundary conditions for RANS simulation.

The mesh is fully unstructured with about 55 K nodes and refined in the near injection region in order to correctly capture the shear layer between the oxygen and hydrogen streams. Table 1 summarizes the operating conditions of the simulated load point.

Mass flow H ₂ [kg/s]	0.02
Mass flow O ₂ [kg/s]	0.14
Temperature H ₂ [K]	95.3
Temperature O ₂ [K]	110.6
Chamber Pressure [bar]	80

Table 1. Input data for the simulation. They correspond to the operating conditions of the simulated load point.

After running the steady state simulation, the radially averaged speed of sound profile and density were interpolated on a cylindrical domain with a diameter of 80 mm, matching the real experimental combustor. The acoustic modes of the chamber volume were estimated with the commercial software COMSOL® Multiphysics using the Helmholtz solver. The nozzle was modeled with an impedance boundary condition to calculate the 1T mode. The 3D solution of the pressure distribution for the 1T mode was used to create a pressure disturbance profile which could be superimposed to the mean pressure on the single injector subdomain in order to simulate the 1T mode excitation of the single injector in the outer row.

In order to apply the presented method, the results of the 2D excited simulations were interpolated on a 3D cylindrical domain representative of the single injector domain volume. Subsequently, the algorithm was applied to get the intensity of the light captured by the probe and compare the obtained signal with the experimental data.

Figure 4 shows the speed of sound, density and OH distribution resulting from the RANS calculation.

Speed of sound and density distribution are then radially averaged in order to obtain a distribution of the variables along the axis to be subsequently interpolated on a cylindrical domain. Then, the Helmholtz equation in the new domain is solved in COMSOL® and the corresponding eigenfrequencies and eigenmodes are obtained. Figure 5

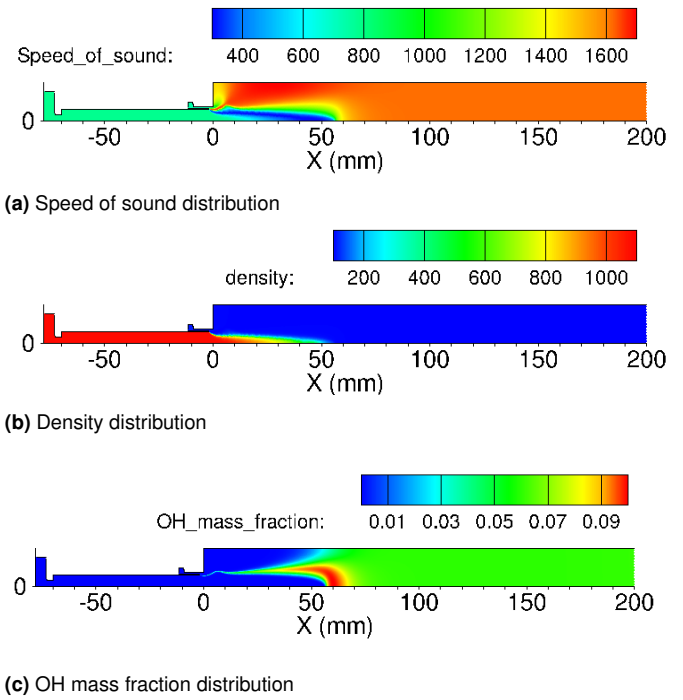


Figure 4. Distribution of the relevant variables for acoustic analysis and radiation model.

shows the profiles of the variables along the axis and the resulting 1T mode profile. Table 2 summarizes the relevant calculated and experimental eigenfrequencies.

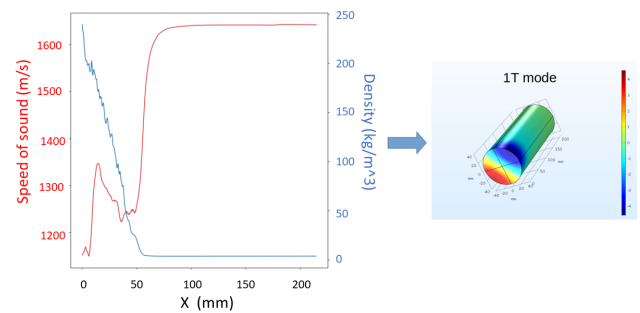


Figure 5. Radially averaged speed of sound and density distribution along the axis and resulting 1T mode.

	Simulation	Experiment
1T mode [Hz]:	11700	10220
2T mode [Hz]:	17667	16680
1R mode [Hz]:	21224	20460
3T mode [Hz]:	22940	22780

Table 2. Frequencies of the relevant eigenmodes of the chamber calculated with COMSOL®.

The procedure described above provides the frequency of the excitation which has to be imposed on the domain to model the 1T mode excitation. Once that the frequency of the excitation has been determined, the pressure disturbance profile has to be imposed on the numerical domain. The disturbance is imposed as an harmonic fluctuation

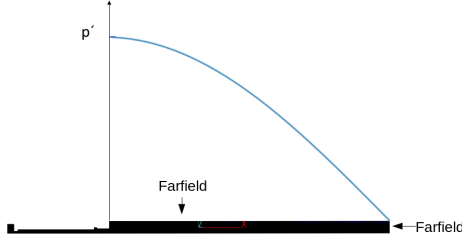


Figure 6. Axial profile of the pressure disturbance imposed on the computational domain p'

at the excitation frequency f with amplitude A given by the experimental data. As it can be seen from Table 2, the simulated frequencies does not match perfectly the experimental ones. This is probably due to the boundary conditions used in the acoustic simulation, which have to be improved to have a better match.

$$p = \bar{p} + p' \quad (5)$$

where p' has the form of:

$$p' = A \cos\left(\frac{\pi x}{2L}\right) \quad (6)$$

where L denotes the length of the domain. In order to impose the pressure disturbance, the inviscid wall boundary condition used on the domain for the RANS simulation has to be replaced with a farfield boundary condition. It is used here to represent an internal fluid boundary and it is defined by specifying the mixture properties at every point on the boundary surface and it allows to impose a distribution of properties along the boundary surface. Figure 6 shows a sketch of the imposed excitation profile of the magnitude of the unsteady pressure along the domain boundary.

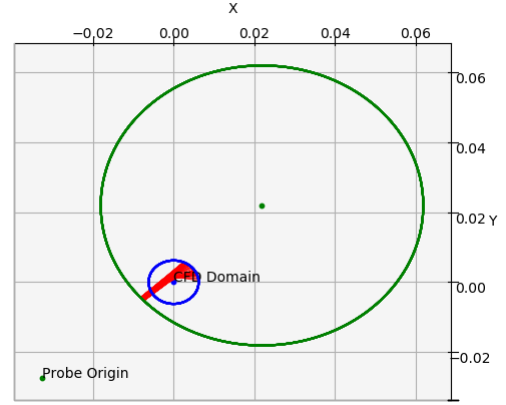
Probe Modelling

Before running SMART on the results of the URANS simulation, a modelling of the optical probe which captures the light is needed, in particular of the view angle. The view angle of the probe is determined by the rays that reach the circular boundary of the fiber-optics face. The probe is approximated to an observation cone with a vertex representing a sink for radiation, indicated with B . The probe surface is assumed to be non-reflective. The total radiation reaching the probe is then obtained by equation 7:

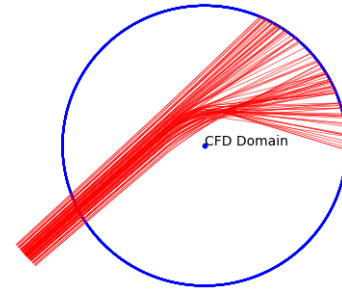
$$\phi(B) = \int_0^\infty \int_\Omega \tau_{\nu,OH} I_\nu(B, \vec{u}) |\vec{u} \cdot \vec{n}_B| d\Omega d\nu \quad (7)$$

where τ_ν , \vec{u} , \vec{n}_B and Ω are the probe's transmissivity function of the wavenumber ν , the radiation direction vector, the normal unit vector of the surface at point B (considered as the probe's pointing vector) and the solid angle given by the observation cone, respectively. I_ν represents the integrated total radiance.

Figures 7a and 7b show the relative location of the BKD chamber and CFD domain boundary and the cross-section view of the trajectory of the rays, respectively. The origin of the observation cone which identifies the probe domain is indicated in figure 7a as Probe Origin. Radiation coming from other surrounding flames is neglected as it is assumed that the radiation detected by the selected probe would come mostly from the flame located at injector 10.



(a) Geometry of the global domain.



(b) Geometry of the CFD domain.

Figure 7. Schematics of the domain geometry with rendered ray paths.

Results

Figure 8 shows the flux of the OH* radiation signal collected by the probe together with the applied pressure disturbance fluctuations.

It can be seen that radiation has a major frequency component of the same value as the pressure with a phase difference smaller than $\pi/2$. Higher and lower frequency components are also visible. To try and explain the presence of these components, a PSD analysis of the OH* radiation signal is compared to the normalized average pressure \bar{p} and density $\bar{\rho}$ signals, as shown in Figure 9.

The peak at $f \approx 11800$ Hz is close to the calculated frequency of the 1T mode $f_{1T} = 11700$ Hz and it is distinguishable in all the three signals. The next observable peaks can be considered as overtones. Focusing on the OH* radiation signal, the power content of the peaks shown in Figure 9 is similar and this explains the complexity of the signal displayed in Figure 8.

Focusing on the range up to 10 kHz, the OH* radiation signal shows a peak at $f \approx 5400$ Hz. Based on the experimental investigation conducted by Armbruster et al.²⁵, it is reasonable to state that this peak corresponds to the 1L

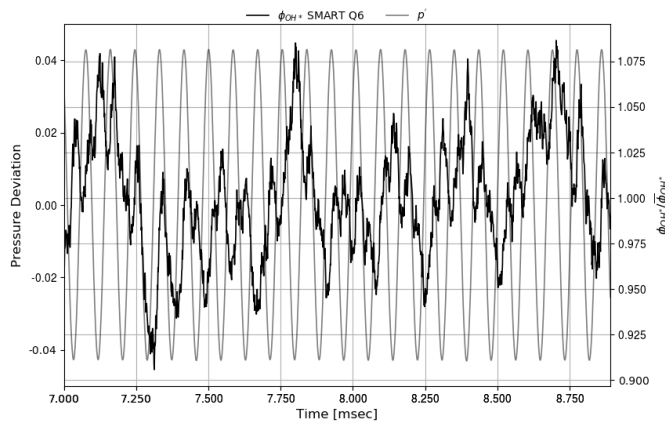


Figure 8. Normalized OH* radiation vs. pressure fluctuations

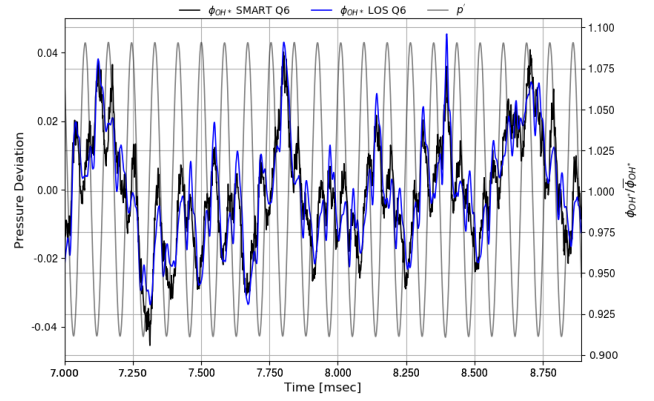


Figure 10. Comparison and difference of the OH* radiation flux signal with LOS approach and SMART.

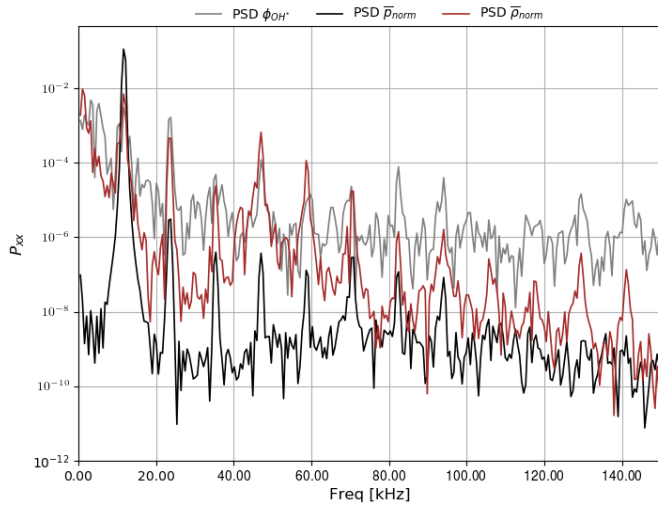


Figure 9. PSD of the OH* radiation signal, average pressure and average density fluctuations.

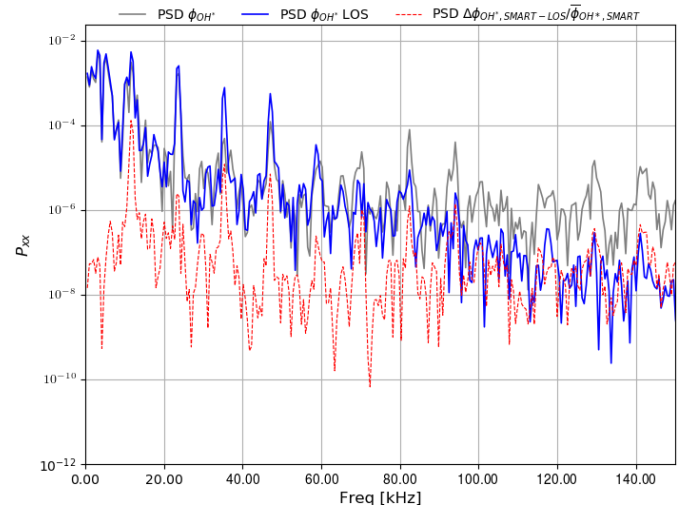


Figure 11. Comparison of the PSD of the OH* radiation flux signal with LOS approach and SMART and of the difference of the two.

mode frequency of the LOx post. This frequency is present as an overtone of the the imposed excitation frequency and then it becomes visible because the LOx post hydrodynamics is excited causing the 1L mode to appear in the frequency content collected by the radiation. This explains why the oscillations of the OH* radiation flux signal are slower than the corresponding pressure fluctuations.

Tonti et al. already investigated the influence of refraction in pseudo-OH* imaging of transcritical flames²⁶ and the same approach was followed in the present study. The comparison is then made between Line-Of-Sight (LOS) simulation where refraction is neglected and the rays follow a straight path through the combustion zone and fully ray-traced images produced with SMART where the bending of the rays, and then refraction, is included. Figure 10 shows the OH* radiation flux signal for both cases normalized to the respective average values.

In general, the trend of the LOS signal follows the one of SMART, although the signal produced by SMART appears to be slightly more complex. When subtracting the radiation flux produced with the LOS approach to the one by SMART, the difference ranges between -4% and +3% of the average radiation flux value. Also the difference between the two signals has a major peak corresponding to the excitation frequency. This is shown in Figure 11, representing the PSD

of the OH* radiation flux calculated via the LOS and the SMART approach and the difference of the two signals.

The PSDs of both SMART and LOS results are similar until $f \approx 90$ kHz: From this value, the LOS PSD starts to decrease in power and the two signals start to differ. Even though the PSD results are similar, it is seen that the frequency composition of their difference peaks are at different overtones of the excitation frequency.

The source of these higher frequency components is then studied more in detail. When investigating the interaction between the rays and the density field, it is seen that the radiation flux oscillations might originate in the interaction of the rays with the wakes of the boundary of the LOx jet. The optical probe directly points to the shear layer between the LOx core and the hydrogen stream and most of the rays pass through this region, and a significant part of the rays crosses the LOx jet wake. Being the shear layer a zone where strong density gradients are encountered both in axial and radial direction, this structure has a frequency content which includes both low and high frequencies. High density gradients result in large refraction index gradients, thus causing the bending of the rays. The rays are bent not only in the radial direction but also in the axial, as shown for one snapshot in Figure 12, and consequently it

changes the intersection of the rays with the OH rich shear layer, as shown in Figure 13. This provides the information that a high frequency component in the rays behaviour is present as well, together with a lower frequency content which describes the translational movement of the wake and at a frequency coincident with the excitation frequency. This would explain why the results obtained with SMART and LOS differ for this peak value of the frequency.

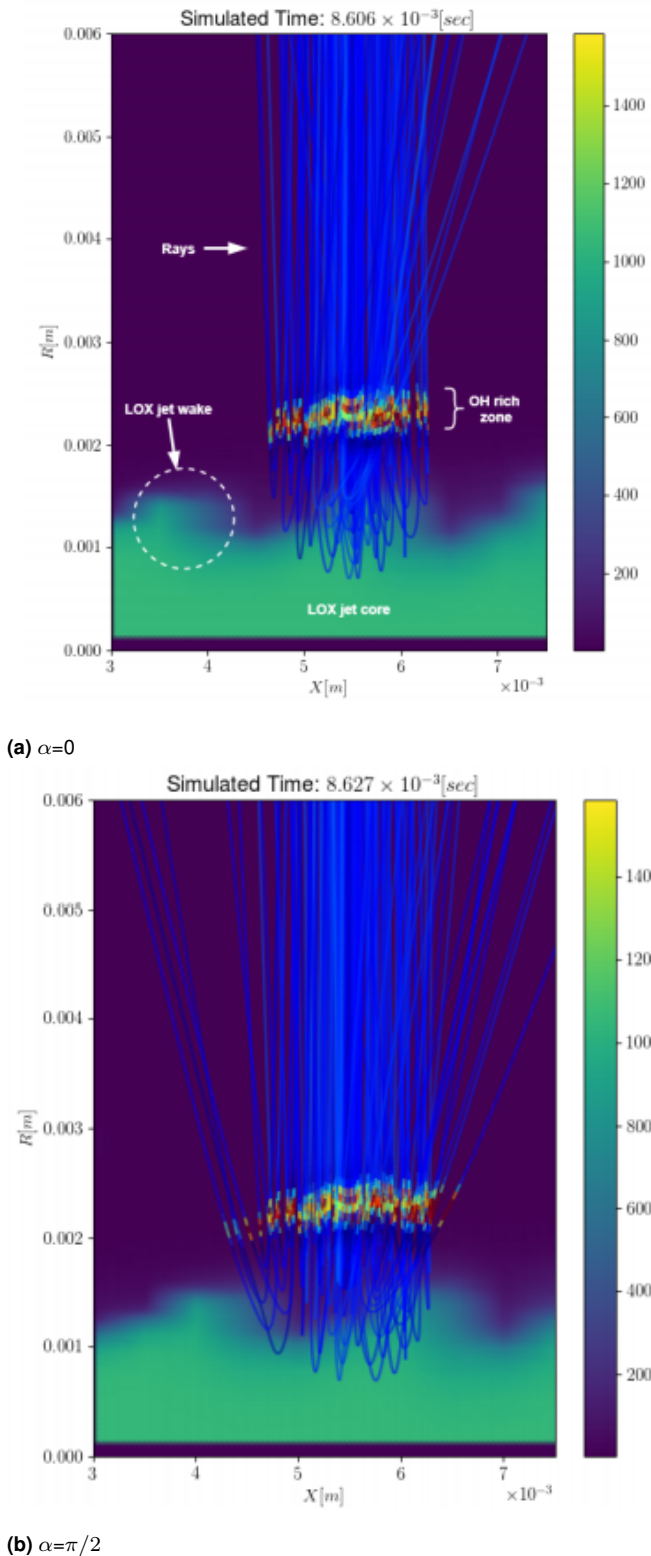


Figure 12. Density distribution and ray paths at different phase angles of the cycle

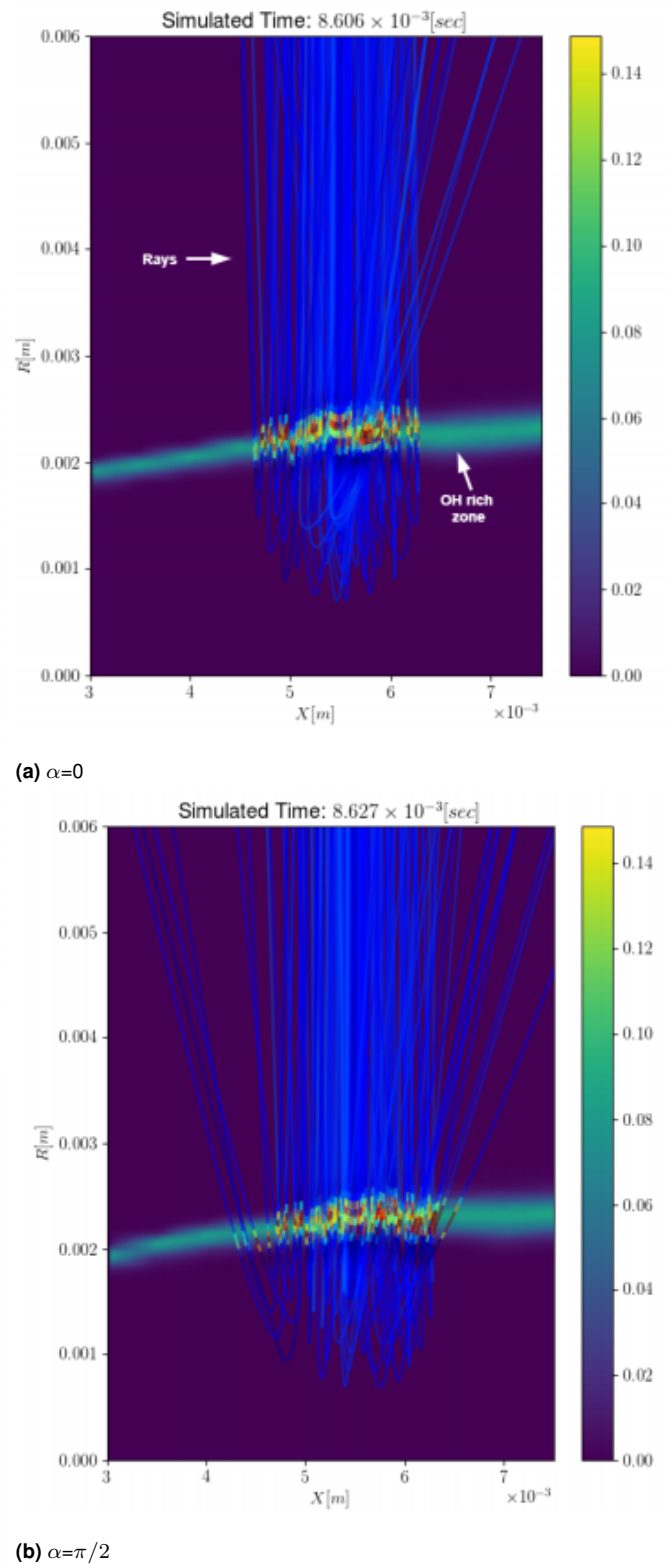


Figure 13. OH mass fraction distribution and ray paths at different phase angles of the cycle

Conclusions and outlook

For the present study, REST test case HF-9, representative of a subdomain of a combustion chamber fed with LOx and H_2 , was used to test the application of the SMART algorithm to an application where an optical probe was used to detect the intensity of the OH* radiation signal. A simple model for an optical probe accounting for the internal

refraction occurring in the sapphire rod was developed with an angle of observation of the cone of 2.39° . The estimated OH* radiation flux signal was investigated. The signal has a major component at the excitation frequency of the pressure field, which corresponds to the estimated 1T mode frequency of the combustion chamber. Additionally, a lower frequency peak is observed at $f \approx 5.4$ kHz which is reasonable to consider the 1L mode of the LOX post, as this has been modeled in the URANS simulations. Predominant higher frequencies observed were found to correspond to overtones of the excitation frequency. A comparison between the SMART and line-of-sight (LOS) results show that both follow a similar trend. The first presents higher frequency components. The difference between the two signals shows that the maximum deviation is $\approx 4\%$ of the mean radiation flux. This deviation occurs at a frequency which corresponds to the excitation frequency and its overtones. The effects of including refraction are visible when performing a PSD analysis, as it impacts the spectral power distribution of the OH* radiation flux signal on the overtones of the excitation frequency. Rays are refracted when passing through the LOX jet wake. The main frequency component is linked to the wake traslation movement, corresponing to the excitation frequency. Turbulent structures with a higher frequency component in the shear-layer result in spatial scattering of the rays which alters their path through the OH rich zones modifying the overall intensity of the signal. OH rich zones do not modify their spatial structure. This leads to the conclusion that refraction may play a role in the frequency composition of the radiation signal collected by the probe. SMART allowed to perform this analysis and gain more insights about the flame dynamics under excitation using the intensity of the radiation of OH* fluctuations. A quantitative approach using a DMD analysis and the parametric study of refraction and OH rich shear layer composition of both effects should be conducted to have further details about this phenomenon.

References

1. Bedard MJ, Fuller TL, Sardeshmukh S et al. Chemiluminescence as a diagnostic in studying combustion instability in a practical combustor. *CombustFlame* 2020; 213: 211–225.
2. Sardeshmukh SV, Bedard M and Anderson WE. The use of OH* and CH* as heat release markers in combustion dynamics. *International Journal of Spray and Combustion Dynamics* 2017; .
3. Liu Y, Tan J, Wan M et al. Quantitative measurement of OH* and CH* chemiluminescence in jet diffusion flames. *ACS Omega* 2020; .
4. Price RB, Hurlle RL and Sugden TM. Optical studies of the generation of noise in turbulent flames. *Symp Combust* 1969; 12(1): 1093–1102.
5. Hornstein B, Budnik C and Courtney W. Research study of light emission caused by pressure fluctuations in rocket engines. Final Report 5520-F, AFOSR, 1966.
6. Farhat SA, Ng WB and Zhang Y. Chemiluminescent emission measurement of a diffusion flame jet in a loudspeaker induced standing wave. *Fuel* 2005; 84(14-15): 1760–1767. DOI: 10.1016/j.fuel.2005.03.020.
7. Freitag E, Konle H, Lauer M et al. Pressure Influence on the Flame Transfer Function of a Premixed Swirling Flame. *Turbo Expo: Power for Land, Sea, and Air* 2006; Volume 1: Combustion and Fuels, Education: 477–486.
8. Lauer M and Sattelmayer T. On the adequacy of chemiluminescence as a measure for heat release in turbulent flames with mixture gradients. *Turbo Expo: Power for Land, Sea, and Air* 2009; Voume 2: Combustion, Fuels and Emissions: 535–544. DOI:10.1115/GT2009-59631. URL <https://doi.org/10.1115/GT2009-59631>. https://asmedigitalcollection.asme.org/GT/proceedings-pdf/GT2009/48838/535/2764101/535_1.pdf.
9. Hardalupas Y and Orain M. Local measurements of the time-dependent heat release rate and equivalence ratio using chemiluminescent emission from a flame. *Comb Flame* 2004; 139: 188–207. DOI:10.1016/j.combustflame.2004.08.003.
10. Hardi JS. *Experimental investigation of high frequency combustion instability in cryogenic oxygen-hydrogen rocket engines*. PhD Thesis, University of Adelaide, Australia, 2012.
11. Lee JG and Santavicca AD. Experimental diagnostics for the study of combustion instabilities in lean premixed combustors. *Journal of Propulsion and Power* 2003; 19(5): 735–750.
12. Wasle H, Winkler A, Lauer M et al. Combustion noise modeling using chemiluminescence data as indicator for the heat release distribution. *European Combustion Meeting* 2007; .
13. Wierman M, Nugent N and Anderson W. Combustion response of a lox/lch4 element to transverse instabilites. *47th AIAA/ASME/SAE/ASEE Joint Propulsion Conference Exhibit, American InSTITUTE of Aeronautics and Astronautics* 2011; .
14. Katrothia T, Riedel IU and Warnatz J. A numerical study on the relation of OH*, CH* and C₂* chemiluminescence and heat release. *Proc Europ Combust Meet* 2009; .
15. Haber LC, Vandsburger U, Saunders WR et al. An experimental examination of the relationship between chemiluminescent light emissions and heat-release rate under non adiabatic conditions. *Proceedings of IGTI* 2000; (2000-GT-0121).
16. Zhang F, Zirwes T, Habisreuther P et al. A dns analysis of the correlation of heat release with chemiluminescence emissions in turbulent combustion. *High Perform Comput Sci Eng'16* 2016; : 229–243.
17. Fiala T. *Radiation from high pressure hydrogen-oxygen flames and its use in assessing rocket combustion instability*. PhD Thesis, Technische Universität München, 2015.
18. Burrows MC. Radiation processes related to oxygen-hydrogen combustion at high pressures. *Symp Comb* 1965; : 207–215.
19. Perovšek J. *Ray Tracing and Spectral Modeling of Excited Hydroxyl Radiation from Cryogenic Flames in Rocket Combustion Chambers*. Master's Thesis, LuleåUniversity of Technology, Department of Computer Science, Electrical and Space Engineering, 2018.
20. Zhu XL and Gore JP. Radiation effects on combustion and pollutant emission of high-pressure opposed flow methane/air diffusion flames. *CombustFlame* 2005; 141(1-2): 118–130.
21. Zhu XL, Gore JP, Karpetis AN et al. The effects of self-absorption of radiation on an opposed flow partially premixed flame. *CombustFlame* 2002; 129(3): 342–345.
22. Gladstone JH and Dale TP. XIV. researches on the refraction, dispersion, and sensitiveness of liquids. *Philosophical Transactions of the Royal Society of London* ; 153.

23. Born M and Wolf E. *Principles of Optics: Electromagnetic Theory of Propagation, Interference and Diffraction of Light (7th Edition)*. 7th ed. Cambridge University Press, 1999. ISBN 0521642221,9780521642224.
24. Gröning M. *Untersuchung selbsterregter Verbrennungsinstabilitäten in einer Raketebrennkammer*. PhD Thesis, RWTH Aachen University, 2017.
25. Armbruster W, Hardi JS, Suslov D et al. Injector-driven flame dynamics in a high-pressure multi-element oxygen–hydrogen rocket thrust chamber. *Journal of Propulsion and Power* 2019; 35(3): 632–644.
26. Tonti F, Perovšek J, Zapata Usandivaras J et al. Obtaining pseudo-OH* radiation images from cfd solutions of transcritical flames. *Combustion and Flame* 2021; .

Copyright statement

Please be aware that the use of this L^AT_EX 2_ε class file is governed by the following conditions.

Copyright

Copyright © 2021 SAGE Publications Ltd, 1 Oliver’s Yard, 55 City Road, London, EC1Y 1SP, UK. All rights reserved.

Acknowledgements

This work is associated with the Franco-German Rocket Engine Stability initiative (REST).